mater.scichina.com link.springer.com

Published online 4 August 2020 | https://doi.org/10.1007/s40843-020-1393-2
Sci China Mater 2021, 64(2): 296–306

$Al_4B_2O_9$ nanorods-modified solid polymer electrolytes with decent integrated performance

Xiqiang Guo[1], Wenjie Peng[1,2], Yuqi Wu[1], Huajun Guo[1,2], Zhixing Wang[1,2], Xinhai Li[1,2], Yong Ke[1,3], Lijue Wu[3], Haikuo Fu[3] and Jiexi Wang[1,2*]

ABSTRACT With the proliferation of energy storage and power applications, electric vehicles particularly, solid-state batteries are considered as one of the most promising strategies to address the ever-increasing safety concern and high energy demand of power devices. Here, we demonstrate the $Al_4B_2O_9$ nanorods-modified poly(ethylene oxide) (PEO)-based solid polymer electrolyte (ASPE) with high ionic conductivity, wide electrochemical window, decent mechanical property and nonflammable performance. Specifically, because of the longer-range ordered Li^+ transfer channels conducted by the interaction between $Al_4B_2O_9$ nanorods and PEO, the optimal ASPE (ASPE-1) shows excellent ionic conductivity of 4.35×10^{-1} and 3.1×10^{-1} S cm^{-1} at 30 and 60°C, respectively. It also has good electrochemical stability at 60°C with a decomposition voltage of 5.1 V. Besides, the assembled $LiFePO_4$//Li cells show good cycling performance, delivering 155 mA h g^{-1} after 300 cycles at 1 C under 60°C, and present excellent low-temperature adaptability, retaining over 125 mA h g^{-1} after 90 cycles at 0.2 C under 30°C. These results verify that the addition of $Al_4B_2O_9$ nanorods can effectively promote the integrated performance of solid polymer electrolyte.

Keywords: all-solid-state lithium ion battery, $Al_4B_2O_9$ nanorods, ionic conductivity, polymer electrolyte

INTRODUCTION

Lithium-ion batteries (LIBs) have been considered as the dominant power devices for their high energy density, long cycle performance and perfect energy transfer efficiency [1]. Currently, the liquid organic electrolyte is widely applied to the commercial LIBs from mobile phone to electric vehicles [2–4]. However, the dilemma is magnified during the pursuit of higher energy density of LIBs because the liquid organic electrolyte contains salts ($LiPF_6$) and flammable organic solvents such as ethylene carbonate (EC) and dimethyl carbonate (DMC). These substances suffer from the problems such as poor electrochemical and thermal stabilities and unpredictable combustion even explosion [5–7].

To address the potential safety concerns, solid-state electrolytes (SSEs) are regarded as one of the most promising substitutes for their decent properties [8–10]. Ideally speaking, compared with the liquid organic electrolyte, SSEs have higher lithium-ion conductivity [11], stronger mechanical performance, higher melting and flammable points, and good chemical and electrochemical stabilities within wider operation windows [12–15]. In general, SSEs can be divided into inorganic electrolytes and polymer electrolytes. Sulfide and oxide electrolytes are the most common and popular types of inorganic electrolytes [16,17], which have relatively high ambient-temperature ionic conductivity (about 10^{-3} to 10^{-2} S cm^{-1}). However, there are so many unsolved problems, such as tremendous interface resistance and poor interface compatibility with present electrodes, which limit their further commercial application [1–22]. On the contrary, the solid polymer electrolytes (SPEs) have excellent chemical and thermal stabilities and good compatibility with electrode materials [23–25]. Significantly, they can be easily and economically manufactured in the conventional production process of LIBs. However, SPEs like poly(ethylene oxide) (PEO) have low ambient-temperature ionic conductivity (~10^{-6} S cm^{-1}) and poor mechanical strengthen. Tremendous efforts have been made to develop suitable SPEs [26,27]. To date, PEO-based SPEs have raised the most intensive attention that aims to address these issues [28]. The matrix structure of

[1] School of Metallurgy and Environment, Central South University, Changsha 410083, China
[2] Engineering Research Center of the Ministry of Education for Advanced Battery Materials, Central South University, Changsha 410083, China
[3] Guangdong Jiana Energy Technology Co. Ltd., Qingyuan 513056, China
* Corresponding author (email: wangjiexikeen@edu.edu.cn)

PEO is highly ordered and exhibits a semi-crystalline state below 60°C, and the crystallization zone of PEO inhibits the transport of ions [29,30]. Therefore, the modification of PEO-based SPEs mainly focus on how to reduce the crystallinity of PEO to improve the ionic conductivity. Considerable methods have been adopted, such as adding plasticizers [24] and inorganic additives [31], comb modifying [32], cross-linking [33,34], block copolymerization [35,36] and polymer blending [37]. Embedding nanomaterials into SPEs was firstly reported by Steele and Weston in 1982 [38]. After that, various metal oxides and other compounds were added as additives into SPEs, such as Al_2O_3 [39], ZrO_2 [40], SiO_2 [41–43], ZnO [44], Fe_3O_4 [45], metal-organic framework (MOF) [46–48], MXene [49], halloysite nano-clay [50], carbon nanotubes [51], and graphene oxide [52]. These additives generally achieve the purpose of reducing the crystallinity of the polymer and enhancing mechanical properties. In addition, it is found that a new ion conduction path exists on the surface of the nanostructured additives, greatly enhancing the ion transport rate of SPEs. To further prove this theory, many researchers pay attention to designing the structure of inorganic additives to construct a continuous network. Cui's group [53,54] claimed that the ordered nanowires provided continuous ion-conducting channels, and the obtained conductivity was much larger than that of SPEs with the random arrangement of nanowires. Besides, Yu and co-workers [55] designed high-performance SPEs with a $Li_{0.35}La_{0.55}TiO_3$ (LLTO) framework derived from a three-dimensional (3D) nanostructured hydrogel, achieving an enhanced Li-ion conductivity of about 8.8×10^{-5} S cm^{-1} at ambient temperature. Then, Fu *et al.* [56] applied 3D network $Li_{6.4}La_3Zr_2A_{10.2}O_{12}$ (LLZO) nanowires to construct SPEs that were able to withstand high voltage and high ignition point, and effectively inhibited the shuttle effect of sulfur cathodes. After that, Tao's group [57] fabricated $Mg_2B_2O_5$ nanowires to increase the Li^+ migrating pathway of SPEs, and the resulting composite SPEs exhibited excellent electrochemical performance. Hence, the smart structural design of the additive is an effective strategy for the development of SPEs.

In this work, we report the synthesis of $Al_4B_2O_9$ (ABO) nanorods by a cost-effective sol-gel method and the fabrication of PEO-based SPEs by inserting ABO to PEO matrix (ASPEs). ABO has excellent mechanical properties, high modulus of elasticity, good flame-retardant property and high applicability [58], and is widely employed as the strengthening material and active additive. With the refractory additive adopted, the fire-resistant performance and the mechanical properties of the SPEs can be enhanced. Besides, the effect of the 1D structure of ABO on improving the lithium-ion transport in ASPE is illustrated. The ASPE-based LIBs are fabricated and deliver outstanding rate performance and long cycle life at 30–60°C.

EXPERIMENTAL SECTION

Preparation of ABO nanorods

ABO nanorods were synthesized by applying sol-gel method to stir aluminum nitrate nonahydrate ($Al(NO_3)_3\cdot 9H_2O$, 98%), boric acid (H_3BO_3) and citric acid ($C_6H_8O_7$) in deionized water for 30 min, and the solution was mixed uniformly and dried at 150°C to gain a pale yellow dry gel. Then the gel was ground into powder and calcined at 900°C for 4 h at a heating rate of 2°C min^{-1}. Finally, the obtained white powder was washed with hot water for three times followed by drying at 60°C to obtain the final product.

Preparation of ASPEs

The ASPEs were prepared by solution casting method. The PEO (M_W=4×10^6, 99.9%) and the lithium bis(trifluoromethane sulfonyl)imide (LiTFSI, +99.5%) were stored in glovebox at argon atmosphere. Firstly, LiTFSI was added to acetonitrile (CH_3CN, AR) and stirred for 1 h. The molar ratio of Li to EO was controlled to be 10 (Li:EO=10:1) according to literature [46]. Then, ABO was added into the solution followed by ultrasonic treatment for 20 min along with stirring for 30 min. After that, the dispersal of PEO continued for 24 h to gain the homogeneous sticky solution. Finally, the solution was cast to a smooth membrane and dried for 24 h in the argon-filled glovebox. Here, the thickness of the membrane was about 80–110 μm with the diameter of 19 or 21 mm. The obtained membranes were named as ASPE-0, ASPE-1, ASPE-2 and ASPE-3 when the weight ratios of ABO in the composite were controlled at 0%, 10%, 20% and 30%, respectively. The composite membranes were put into a vacuum drying oven at 80°C to remove moisture before physical characterization and cell assembly.

Structural characterizations

The X-ray diffraction (XRD, Rigaku, TTR III equipped with Cu target, $\lambda_{K\alpha}$=1.54184 Å; 40 kV, 250 mA) was applied to determine the purity of additive, and crystalline phases and crystallinity degree of the synthesized membrane electrolytes. The microscopic structure of ABO and the surface morphologies of the modified SPEs were ob-

served with a scanning electron microscope (SEM, MIRA3 LMH, TESCAN). Energy disperse spectroscopy (EDS) analysis and element mapping were carried out on an Oxford X MAX20 of TESCAN. The functional group information was investigated by using Fourier Transform-infrared spectroscopy (FTIR, Nicolet 380, Thermo Nicolet Corporation with KBr tablet).

DSC measurement and tension test

Differential scanning calorimetry (DSC) measurement was tested on DSC214 (NETZSCH) in the temperature range of −50–160°C with a heating rate of 10°C min^{-1} in N_2 atmosphere. According to the phase transition peak of the DSC profiles of SPEs, the crystallinity melting point of the polymer (T_m) and enthalpy of fusion (ΔH_m) were roughly obtained. The enthalpy of fusion of PEO at complete crystallinity (ΔH_0) is 213.7 J g^{-1}. The crystallinity degree (X_c) of SPEs was estimated by using the equation: $X_c = \Delta H_m/\Delta H_0$ [59]. Biomechanical tension testing machine (23 MTS Insight) was applied to compare the relationship between the maximum stress and the strain value of SPEs.

Cell assembly and electrochemical tests

Li symmetrical cells, steel symmetrical cells, Li//steel cells and $LiFePO_4$//Li (LFP//Li) cells with ASPEs as solid electrolytes were assembled in argon-filled glove-box for electrochemical analysis. The LFP-based cathode was prepared by dispersing the active material LFP, carbon black (SP) and polyvinylidene fluoride (8:1:1 by weight ratio) in *N*-methyl pyrrolidone solvent to obtain slurry, which was then coated on Al foil and dried under vacuum at 120°C for 6 h. The active material loading of LFP cathode was 1–2 mg cm^{-1}. The ionic conductivities of ASPEs were tested in the steel symmetrical cells by electrochemical impedance spectroscopy with an alternating current (AC) amplitude of 10 mV in the frequency range of 0.1–10^6 Hz and a temperature range of 30–80°C on an electrochemical station (PARSTAT 4000A). The electrochemical stabilities of ASPEs were measured with linear sweep voltammetry (LSV) at a scanning rate of 5 mV s^{-1} from 0 to 6.0 V in Li//steel cells at ambient temperature. The Li^+ transference number (t_{Li^+}) was evaluated at 60°C by utilizing the electrochemical combination method of direct current (DC) polarization/alternating current impedance in the Li symmetrical cells. The t_{Li^+} value was calculated by using the following equation:

$$t_{Li^+}=[I_s(C\Delta V-I_0R_0)]/[I_0(C\Delta V-I_sR_s)],$$

where ΔV is the applied voltage (10 mV), I_0 and I_s (mA) are the initial current and steady current during the DC polarization process, respectively. R_o and R_s (Ω) are the charge-transfer resistances of Li symmetric cell before and after DC polarization, respectively. The electronic conductivity σ was estimated with the equation:

$$\sigma=l/(S\cdot R_b),$$

where σ (S cm^{-1}) is the ion conductivity when the electronic conductivity could be ignored; l (cm) is the thickness of the electrolyte membrane; R_b (Ω) is the bulk impedance; S (cm^2) is the area of contacting with stainless steel electrode.

RESULTS AND DISCUSSION

High-modulus, fire-resistant and elongated ABO samples were prepared under different temperatures from 700 to 1000°C, and the best calcination temperature is 900°C (Figs S1 and S2). The synthetic route of ABO is illustrated by the processing diagram in Fig. 1a. Fig. 1b shows the typical XRD pattern of the obtained ABO powder, all of the diffraction peaks are well consistent with crystal $Al_4B_2O_9$ (PDF#29-0010), indicating that the high-quality ABO powder is synthesized. SEM images of the ABO are displayed at Fig. 1c and d, where the average diameter of ABO is ~200 nm with well distribution.

As shown in Fig. 2a–c, the surface morphology and structure of ASPE-1 are the same as what we design. Front-view SEM (Fig. 2a) presents that ASPE-1 has certain fold, while it is smoother than that of ASPE-0 (Fig. S3). The thickness of ASPE-1 is about 54 μm (Fig. 2b). In fact, the thickness of ASPE-1 is very important when the membrane electrolyte is used to assemble coin cells, and it is usually controlled between 50 and 65 μm in case of the battery short circuit or the huge integrated resistance. Fig. 2c shows the existence of ABO at the surface of ASPE-1 from the element distribution of the Al, B and O elements in the EDS mapping, which confirm the existence of ABO. It can also be found that the additive is well maintained and orderly scattered in the membrane. Eventually, it will strengthen the mechanical properties of ASPE-1 at a certain degree. This will be discussed in following tension test.

Ionic conductivity is a crucial parameter to assess the electrochemical properties of SPEs. AC impedance spectra of the ASPEs in the steel symmetrical cells at 30–70°C are shown in Fig. 3a and Fig. S4. In the Nyquist plot of ASPE-1 (Fig. 3a), the high frequency region is shown as a compressed semicircle, which is related to the intrinsic impedance of SPEs film and the flatness of SPE/electrode interface. The semicircle is not fully visible because the high-frequency part of the instrument is not high enough. The low-frequency region is a straight line, which is re-

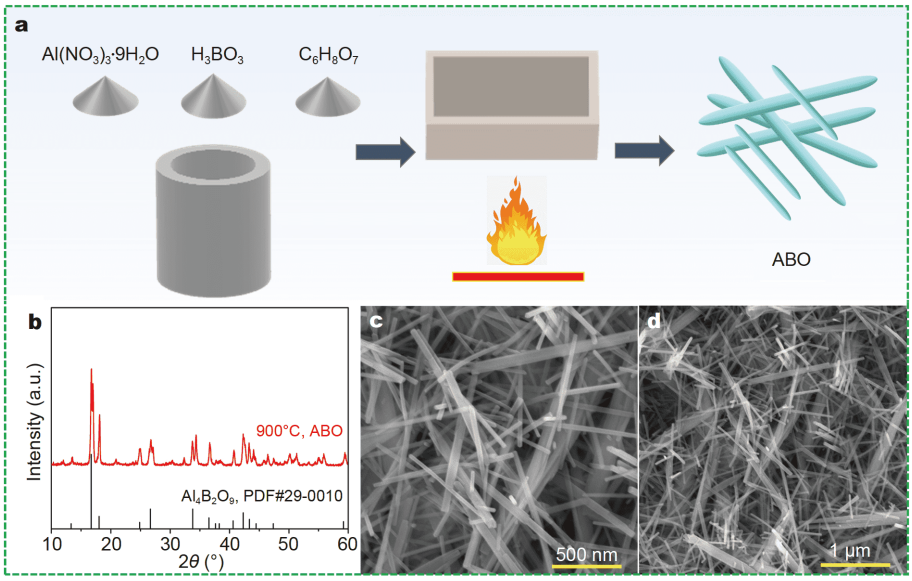

Figure 1 (a) Schematic illustration of the synthetic route of ABO and (b–d) characterization of the ABO: (b) typical XRD curves; (c, d) SEM images.

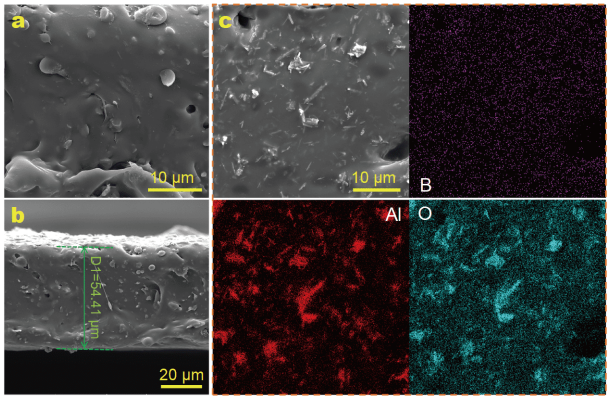

Figure 2 Surface morphologies of ASPE-1: (a) front-view SEM image; (b) cross-sectional SEM image; (c) elemental mappings (B, Al, and O).

lated to lithium ion migration [60]. By calculation, the ionic conductivity of the as-prepared ASPEs can be obtained at 30–70°C. As shown in Fig. 3b, the ionic conductivity of the composite SPEs containing ABO is enhanced remarkably compared with the SPEs without ABO. Among all the ASPEs, the ASPE-1 sample has the highest ionic conductivity of 4.35×10^{-5}, 2.1×10^{-4} and 3.1×10^{-4} S cm^{-1} at 30, 50 and 60°C, respectively. It shows that the ionic conductivity of the electrolyte grows with the increase of temperature. When the content of ABO increases, the conductivity firstly goes up, then drops. The reason may be that excessive ABO is packed in the polymer matrix, resulting in aggregation of ABO nanorods and free volume consumption for ion channels [61]. Therefore, a decrease in ionic conductivity of SPEs occurs. Besides, the lithium-ion conductivity of SPEs also depends on the number of lithium-ion migration [62], which was tested on the electrolyte using the method of AC impedance combined with constant voltage polarization. At the beginning of polarization, the migration of lithium ions and anions transport as a current. When the polarization is stable, only lithium ions are migrated, then the number of lithium ions can be calculated [63]. As shown in Fig. 3c, the ASPE-1 has a lithium-ion migration number of 0.18 at 60°C, much higher than that of bare ASPE-0 (about 0.1). This indicates that the ABO additive can effectively enhance the lithium-ion migration number to improve the overall ion conductivity.

Based on related studies, there is a widely acknowledged theory for explaining the mechanism of ABO addition to enhance the ionic conductivity of ASPEs [57]. As illustrated in Fig. 4a, ABO with opposite electrical properties is able to promote the dissociation of lithium salts into lithium ions and anions. At the surface of ABO, $(NSO_2CF_3)_2^-$ anions in lithium salts may be restricted by Al atom as positively charged centers, while Li^+ can transport between the oxygen-negatively charged centers on ABO and EO units in the PEO polymer segments, which contain a large number of lone pairs of electrons and can interact with Li^+. The interactions of PEO and ABO with Li^+ help to introduce PEO to the surface of ABO and rearrange them, accelerating the "complexation-decomplexation-complexation" process. As a result, the ion-conducting channels are formed *via* the Lewis

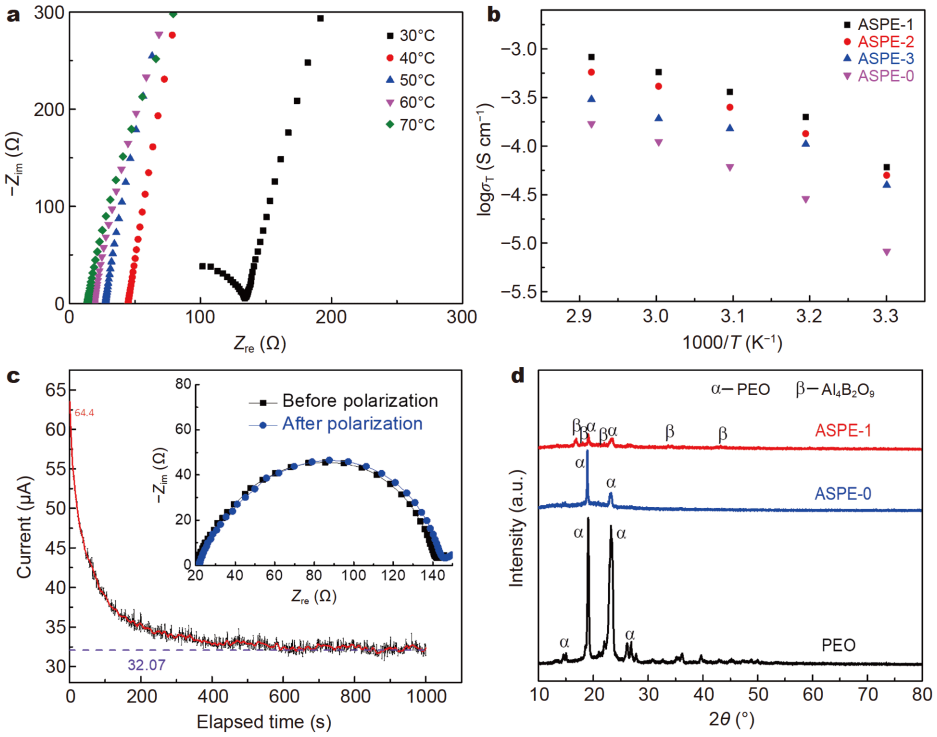

Figure 3 (a) AC impedance spectra of ASPE-1 in the steel symmetrical cells at 30–70°C. (b) Ionic conductivity of ASPEs in the steel symmetrical cells at 30–70°C. (c) DC polarization curves of ASPE-1 in the Li symmetrical cell under 60°C at a potential step of 10 mV. Inset: the AC impedance spectra of the cell before polarization and after steady-state current conditions. (d) Typical XRD patterns of PEO, ASPE-0 and ASPE-1.

acid-base interactions among ABO, LiTFSI and PEO, the transmission distance of free lithium ions decreased, the dissociation ability of lithium salts is enhanced, and the crystallinity of PEO is reduced. Therefore, compared with isolated nanoparticles, continuous nanomaterials can provide longer-range-ordered lithium-ion transport channels, and the conduction of lithium ions is remarkably enhanced [61].

Fig. 4b presents the FTIR of the PEO, LiTFSI, ABO, ASPE-0 and ASPE-1 at 4000–400 cm^{-1}. From the overall infrared spectra, it can be seen that the absorption peak position of the reaction signal for changes of SPE structure maintains in the low-frequency region, so the spectra are focused on the range of 1400–1150 cm^{-1} (Fig. 4c) to enlarge and fit the peaks as much precise as possible. The absorption peaks of ASPE-0 at 1186 and 1351 cm^{-1} shift to 1186 and 1352 cm^{-1} in the infrared spectrum of ASPE-1, respectively. Compared with pure PEO, LiTFSI and ABO, new absorption peaks at 1228 and 1320 cm^{-1} appear and the LiTFSI absorption peak at 1333 cm^{-1} shifts to 1330 cm^{-1} in ASPE-0. The positions and assignments of the relevant fitted infrared spectral peaks are listed in Table 1. According to the assignments of peaks in PEO, LiTFSI and ABO, the newly emerging peaks in ASPE-0 are classified as $-CF_3$ symmetric stretching and $-SO_2-$ asymmetric stretching peaks. The shift of $-SO_2-$ absorption peak and the split of $-CF_3$ peaks indicate that the lithium salt LiTFSI is dissociated in ASPE-0, causing changes in the anionic chemical environment [64]. With the addition of ABO in ASPE-1, the vibrational absorption peak of $-CF_3$ changes significantly, and the $-SO_2-$ asymmetric stretching peak in the lithium salt also shifts. However, the peaks of $-CH_2-$ in PEO remain unchanged. It means that ABO mostly has interactions with $-SO_2-$ group and $-CF_3$ group in $(NSO_2CF_3)_2^-$ anion, thereby promoting the dissociation of lithium salts and forming lithium-ion transmission channels.

Apart from the ionic conductivity, the thermal and mechanical stabilities of SPEs play a significant role in the further application of all-solid-state battery. DSC curves of ASPE-0 and ASPE-1 are presented in Fig. 5a. It can be seen that the crystalline melting points of PEO, ASPE-0 and ASPE-1 are 69.1, 46.5, and 41.6°C, respectively. The addition of ABO can effectively reduce the melting point of PEO, which helps to shift the crystalline region in the polymer to amorphous region [54]. This is the main

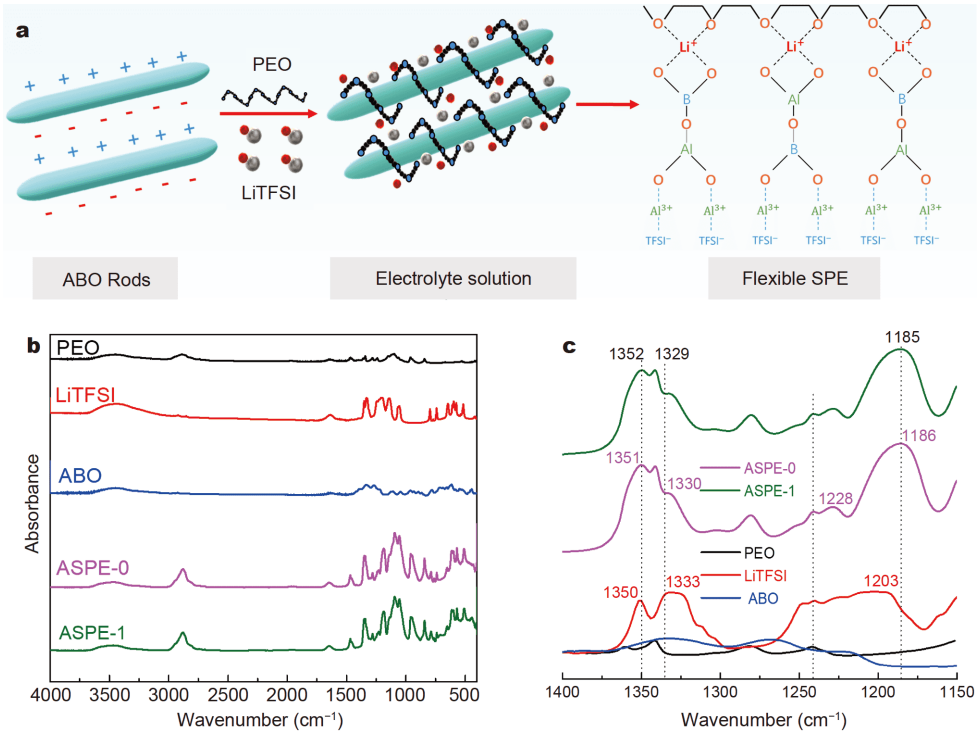

Figure 4 (a) Illustration for mechanism of enhanced ionic conductivity of PEO-based electrolyte with ABO addition. (b, c) FTIR spectra of the PEO, LiTFSI, ABO, ASPE-0 and ASPE-1: (b) 4000–400 cm^{-1}; (c) 1400–1150 cm^{-1}.

Table 1 FTIR peaks and assignments for PEO, LiTFSI, ASPE-0 and ASPE-1

Peak assignment	Wavenumber (cm^{-1})			
	PEO	LiTFSI	ASPE-0	ASPE-1
$-CH_2-$ wagging absorptions in helical structure	1360	1350	1360/1351	1360/1352
$-CH_2-$ wagging absorptions in trans planar structure	1342		1342	1342
$-CH_2-$ twist in helical structure	1280		1280	1280
$-CH_2-$ twist in trans planar structure	1242		1241	1241
Asymmetric $-SO_2-$ stretching		1333	1330/1320	1329/1316
Symmetric stretching of $-CF_3$		1240	1241/1228	1241/1228
Asymmetric stretching of $-CF_3$		1203	1185	1186

reason for the improvement in ionic conductivity. According to the equation $X_c = \Delta H_m/\Delta H_0$ (213.7 J g^{-1}), the corresponding estimated crystallinities of PEO, ASPE-0 and ASPE-1 are 62.7%, 9.5% and 8.5%, respectively. Although this method is not very precise, the result is consistent with the pattern of XRD in Fig. 3c, indicating that the addition of ABO can indeed reduce the crystallinity of PEO [65]. The strength of SPE film is of great significance to prevent the growth of lithium dendrite, so the tension test was conducted by MTS biomechanical testing machine. As shown in Fig. 5b, the plots illustrate that the addition of ABO nanorods increases the maximum stress of the resultant PEO-based SPEs from 1.25 to 1.71 MPa and the maximum deformation strength from 717% to 763%, indicating that the addition of 1D ABO nanorods can improve the mechanical properties of PEO-based SPEs to some extent.

Safety concern of LIBs, which is mainly ascribed to the flammability of organic liquid electrolyte, is considered as the extremely significant part of energy devices' application. Fig. 5c compares the flammability between organic liquid electrolyte, ASPE-0 and ASPE-1 with lighter at a certain distance. When the electrolyte is liquid $LiPF_6$ EC/DMC (1:1 ratio by volume), intense combustion occurs

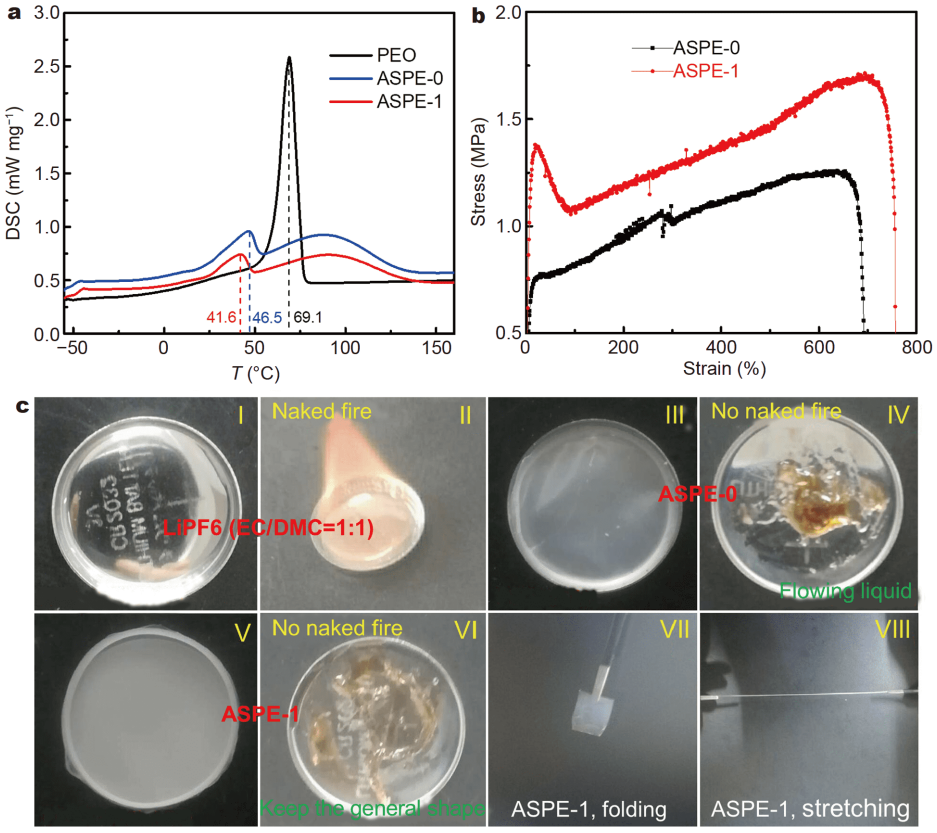

Figure 5 (a) DSC curves of ASPE-0 and ASPE-1 under N_2 atmosphere. (b) Tension tests of ASPE-0 and ASPE-1. (c) Combustion experiments of $LiPF_6$ (EC/DMC=1:1) (I, II), ASPE-0 (III, IV), and and ASPE-1 (V, VI); the folding and stretching experiments of ASPE-1 (VII, VIII).

immediately after contacting with the lighter in Fig. 5c (I, II). Fig. 5c (III, IV) shows that the ASPE-0 demonstrates a small fire for only a few seconds after burning by the lighter, indicating that ASPE-0 is safer than organic liquid electrolyte. However, ASPE-0 cannot keep the original shape, and the liquid material becomes flowable. As for ASPE-1 (Fig. 5c (V, VI)), the general shape will not be changed unless the fire is maintained for several minutes, and the fire goes out immediately when the lighter is taken off. Obviously, with the addition of ABO, the ASPE-1 has a better flame-retardant property with a higher ignition point (Fig. S5). The forms of ASPE-1 after folding and stretching in Fig. 5c (VII, VIII) indicate that ASPE-1 can be flexibly folded and the mechanical property of ASPE-1 is acceptable, which will benefit the long cycle performance of batteries.

It is well-known that the lower value of polarization voltage, the more stable electrolyte/electrodes interface [10]. The polarization curves of Li symmetrical cells with ASPE-0 and ASPE-1 at 60°C under 0.1 mA cm^{-2} are compared in Fig. 6a. The polarization voltage of Li/ASPE-1/Li is lower than that of pristine Li/ASPE-0/Li. Besides, it is extremely steady after 120 h, proving that the addition of ABO can improve the electrochemical stability of SPE/Li interface. Fig. 6b illustrates the polarization cycle of Li symmetrical cells with ASPE-0 and ASPE-1 under different current conditions. At 0.1, 0.2 and 0.3 mA cm^{-2}, the polarization voltages of cells with ASPE-0 are 49, 92 and 143 mV while those with ASPE-1 are 42, 76 and 115 mV, respectively. Besides, the decomposition voltage is one of the essential parameters of the electrochemical characteristics. The high decomposition voltage makes the electrolyte to match with high-voltage cathode materials [36]. As such, the energy density of battery can be improved. LSV profiles of steel//Li cells with ASPE-0 and ASPE-1 films at 10 mV s^{-1} at 60°C are shown in Fig. 6c. The decomposition voltages of ASPE-0 and ASPE-1 are 4.55 and 5.10 V, respectively, which are higher than the decomposition voltage of the liquid electrolyte (about 4.20 V [7]). Although PEO is gradually decomposed over 4 V, with the addition of ABO, the decomposition degree of PEO reduces at high voltage. Ten groups of batteries

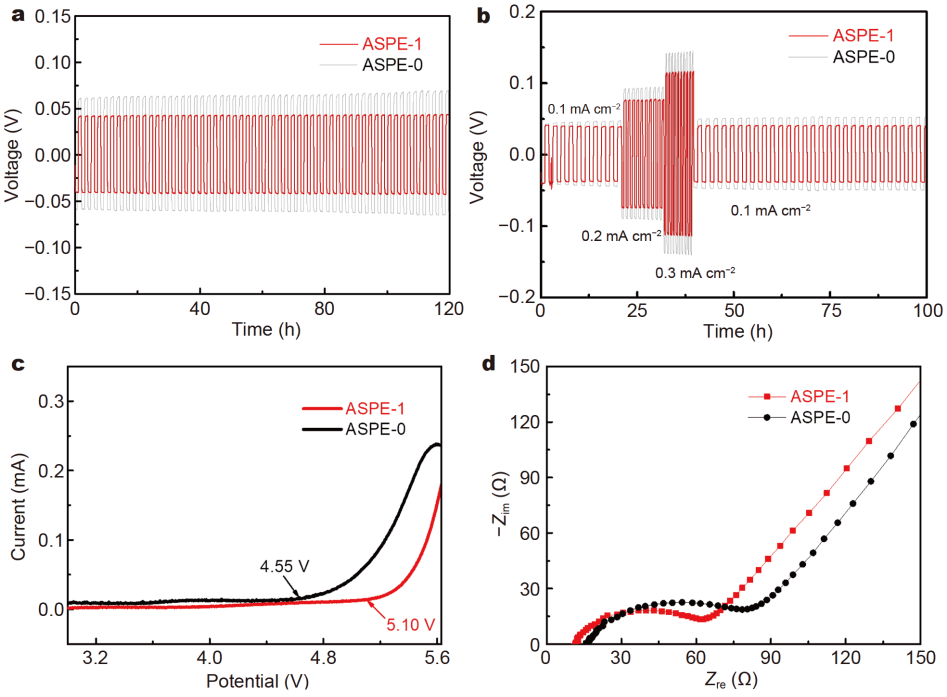

Figure 6 Voltage profiles of Li symmetrical cells with ASPE-0 and ASPE-1 as electrolytes under 60°C at (a) 0.1 mA cm^{-2} and (b) 0.1–0.3 mA cm^{-2}. (c) LSV curves of steel//Li cells with ASPE-0 and ASPE-1 as electrolytes at 10 mV s^{-1} at 60°C. (d) EIS spectra of LFP//Li cells with ASPE-0 and ASPE-1 as electrolyte at 60°C.

were selected for impedance tests at 60°C in LFP//Li system. The most representative average impedance spectra are presented in Fig. 6d. The semicircle in the high-frequency region and the intercept on the real axis represent the charge-transfer resistance (R_{ct}) and the ohmic resistance (R_0), respectively. R_{ct} and R_0 of ASPE-1 are nearly 50.7 and 11.9 Ω, respectively, which are slightly smaller than those of ASPE-0 (65.8 and 16.6 Ω), indicating that the addition of ABO nanorods reduces the impedance of the battery to a certain extent. This reflects that ASPE-1 has higher ionic conductivity and smoother surface to reduce the contact resistance with electrode, which again confirms the positive effect of ABO additive.

The cycling performance of LFP//Li cells with ASPE-0 and ASPE-1 at 60°C is revealed in Fig. 7a–c. Fig. 7a shows the charge/discharge curves of the batteries at different C-rates. The discharge and charge voltage plateaus are around 3.30 and 3.50 V at 0.2 C, respectively. As the current density grows, the gaps between the discharge and charge voltages increase significantly. Fig. 7b shows the cycle performance of cells with ASPE-0 and ASPE-1 at 1 C under 60°C, in which the LFP/ASPE-1/Li cell shows a high specific capacity of 155 mA h g^{-1} after 300 cycles. The capacity increases during initial cycles due to the activation of ASPE-1. Compared with the LFP/ASPE-0/Li cells, there is a remarkable enhancement in electrochemical performance. Fig. 7c shows the specific discharge capacity of LFP/ASPE-1/Li cells is remarkably higher than that of LFP/ASPE-0/Li cells. Particularly, the specific discharge capacities of LFP/ASPE-1/Li cells are 166, 159, 155, 141 and 122 mA h g^{-1} at 0.2, 0.5, 1.0, 2.0 and 4.0 C, respectively. The cycling performance at 0.2 C under 30°C is presented in Fig. 7d. The LFP/ASPE-1/Li cells show a high specific capacity over 125 mA h g^{-1} after 90 cycles, while LFP/ASPE-0/Li cells only delivers 60 mA h g^{-1} in initial 80 cycles and gets short circuit after that due to the growth of lithium dendrites. This proves that the addition of ABO greatly enhances the low-temperature performance of PEO-based SPEs. It also indicates that the ASPE-1 is able to decrease the growth speed of lithium dendrites.

CONCLUSIONS

In summary, by utilizing the elongated ABO, the electrochemical performance of the PEO-based SPEs has been significantly improved. The PEO crystallinity was decreased by the addition of ABO. The interaction between ABO and –SO_2– in the $TFSI^-$ anion promoted the release and transport of lithium ions, thus improving the ionic conductivity. Besides, ABO with excellent me-

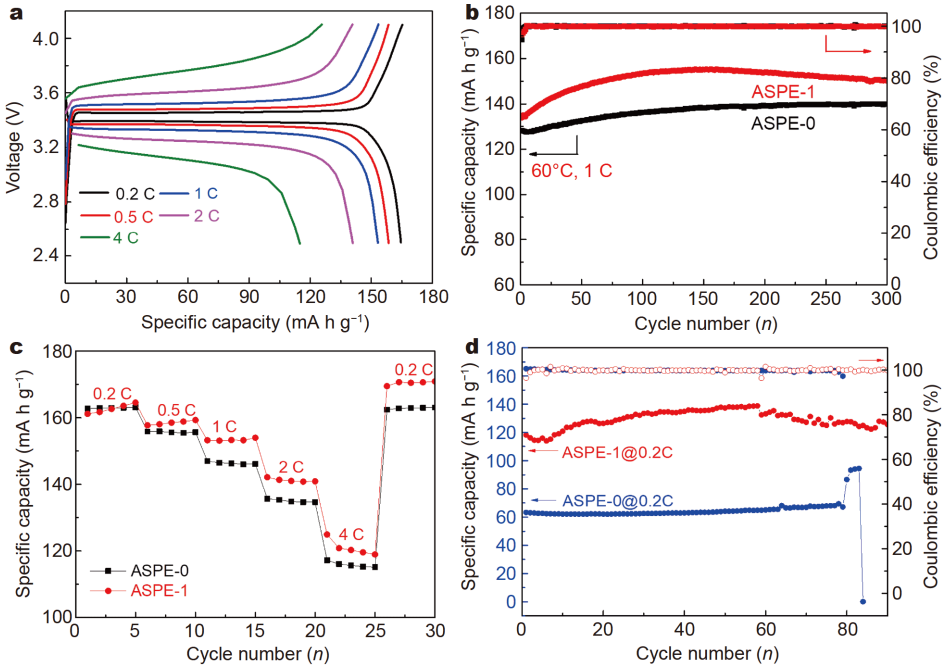

Figure 7 Electrochemical performance of LFP//Li cells with ASPE-0 and ASPE-1 as electrolytes: (a) typical charge–discharge curves at 60°C; (b) cycling performance under 1 C at 60°C; (c) rate performance at 60°C; (d) cycling performance at 0.2 C under 30°C.

chanical strength and fire-resistant property effectively enhanced the integrated performance of composite electrolyte, which had a lower melting point, and flexible and stretchable surface. As a result, the cells assembled with ASPE-1 demonstrated improved cyclic performance and rate capability in a wide temperature range. This work finds an original and meaningful 1D nanomaterial to enhance the integrated properties of PEO-based SPEs, which gives the promising future of such novel but low-cost additive and presents the advance of safe SPEs for possible practical applications.

Received 4 April 2020; accepted 12 May 2020; published online 4 August 2020

1 Li M, Lu J, Chen Z, *et al.* 30 years of lithium-ion batteries. Adv Mater, 2018, 30: 1800561
2 Cao Y, Li M, Lu J, *et al.* Bridging the academic and industrial metrics for next-generation practical batteries. Nat Nanotechnol, 2019, 14: 200–207
3 Chen X, Ma Y. Wearable lithium ion batteries based on carbon nanotubes and graphene. Adv Mater Technol, 2018, 3: 1800041
4 Wang Y, Chen C, Xie H, *et al.* 3D-printed all-fiber Li-ion battery toward wearable energy storage. Adv Funct Mater, 2017, 27: 1703140
5 Palacin MR, de Guibert A. Why do batteries fail? Science, 2016, 351: 1253292
6 Wang J, Yamada Y, Sodeyama K, *et al.* Fire-extinguishing organic electrolytes for safe batteries. Nat Energy, 2018, 3: 22–29
7 Lin D, Liu Y, Cui Y. Reviving the lithium metal anode for high-energy batteries. Nat Nanotech, 2017, 12: 194–206
8 Fan L, Wei S, Li S, *et al.* Recent progress of the solid-state electrolytes for high-energy metal-based batteries. Adv Energy Mater, 2018, 8: 1702657
9 Manthiram A, Yu X, Wang S. Lithium battery chemistries enabled by solid-state electrolytes. Nat Rev Mater, 2017, 2: 16103
10 Nolan AM, Zhu Y, He X, *et al.* Computation-accelerated design of materials and interfaces for all-solid-state lithium-ion batteries. Joule, 2018, 2: 2016–2046
11 Kamaya N, Homma K, Yamakawa Y, *et al.* A lithium superionic conductor. Nat Mater, 2011, 10: 682–686
12 Keller M, Appetecchi GB, Kim GT, *et al.* Electrochemical performance of a solvent-free hybrid ceramic-polymer electrolyte based on $Li_7La_3Zr_2O_{12}$ in $P(EO)_{15}LiTFSI$. J Power Sources, 2017, 353: 287–297
13 Meesala Y, Jena A, Chang H, *et al.* Recent advancements in Li-ion conductors for all-solid-state Li-ion batteries. ACS Energy Lett, 2017, 2: 2734–2751
14 Sun C, Liu J, Gong Y, *et al.* Recent advances in all-solid-state rechargeable lithium batteries. Nano Energy, 2017, 33: 363–386
15 Wang C, Xie H, Ping W, *et al.* A general, highly efficient, high temperature thermal pulse toward high performance solid state electrolyte. Energy Storage Mater, 2019, 17: 234–241
16 Sun YZ, Huang JQ, Zhao CZ, *et al.* A review of solid electrolytes for safe lithium-sulfur batteries. Sci China Chem, 2017, 60: 1508–1526
17 Sharafi A, Kazyak E, Davis AL, *et al.* Surface chemistry mechanism of ultra-low interfacial resistance in the solid-state electrolyte $Li_7La_3Zr_2O_{12}$. Chem Mater, 2017, 29: 7961–7968
18 Nam YJ, Cho SJ, Oh DY, *et al.* Bendable and thin sulfide solid

electrolyte film: a new electrolyte opportunity for free-standing and stackable high-energy all-solid-state lithium-ion batteries. Nano Lett, 2015, 15: 3317–3323
19 Bachman JC, Muy S, Grimaud A, *et al.* Inorganic solid-state electrolytes for lithium batteries: mechanisms and properties governing ion conduction. Chem Rev, 2016, 116: 140–162
20 Dai J, Yang C, Wang C, *et al.* Interface engineering for garnet-based solid-state lithium-metal batteries: Materials, structures, and characterization. Adv Mater, 2018, 30: 1802068
21 Fu KK, Gong Y, Hitz GT, *et al.* Three-dimensional bilayer garnet solid electrolyte based high energy density lithium metal–sulfur batteries. Energy Environ Sci, 2017, 10: 1568–1575
22 Dong D, Zhou B, Sun Y, *et al.* Polymer electrolyte glue: A universal interfacial modification strategy for all-solid-state Li batteries. Nano Lett, 2019, 19: 2343–2349
23 Chen L, Li Y, Li SP, *et al.* PEO/garnet composite electrolytes for solid-state lithium batteries: From "ceramic-in-polymer" to "polymer-in-ceramic". Nano Energy, 2018, 46: 176–184
24 Yang K, Zhang Z, Liao Z, *et al.* Organic ionic plastic crystal-polymer solid electrolytes with high ionic conductivity and mechanical ability for solid-state lithium ion batteries. ChemistrySelect, 2018, 3: 12595–12599
25 Zhang W, Nie J, Li F, *et al.* A durable and safe solid-state lithium battery with a hybrid electrolyte membrane. Nano Energy, 2018, 45: 413–419
26 Hu J, Wang W, Zhou B, *et al.* Poly(ethylene oxide)-based composite polymer electrolytes embedding with ionic bond modified nanoparticles for all-solid-state lithium-ion battery. J Membrane Sci, 2019, 575: 200–208
27 Yuan B, Luo G, Liang J, *et al.* Self-assembly synthesis of solid polymer electrolyte with carbonate terminated poly(ethylene glycol) matrix and its application for solid state lithium battery. J Energy Chem, 2019, 38: 55–59
28 Zhou W, Wang Z, Pu Y, *et al.* Double-layer polymer electrolyte for high-voltage all-solid-state rechargeable batteries. Adv Mater, 2019, 31: 1805574
29 Tan SJ, Zeng XX, Ma Q, *et al.* Recent advancements in polymer-based composite electrolytes for rechargeable lithium batteries. Electrochem Energ Rev, 2018, 1: 113–138
30 Xi J. Electrochemistry study on PEO-$LiClO_4$-ZSM_5 composite polymer electrolyte. Chin Sci Bull, 2004, 49: 785
31 Yao P, Zhu B, Zhai H, *et al.* PVDF/palygorskite nanowire composite electrolyte for 4 V rechargeable lithium batteries with high energy density. Nano Lett, 2018, 18: 6113–6120
32 Ji X, Zeng H, Gong X, *et al.* A Si-doped flexible self-supporting comb-like polyethylene glycol copolymer (Si-PEG) film as a polymer electrolyte for an all solid-state lithium-ion battery. J Mater Chem A, 2017, 5: 24444–24452
33 Lopez J, Sun Y, Mackanic DG, *et al.* A dual-crosslinking design for resilient lithium-ion conductors. Adv Mater, 2018, 30: 1804142
34 Grewal MS, Tanaka M, Kawakami H. Bifunctional poly(ethylene glycol) based crosslinked network polymers as electrolytes for all-solid-state lithium ion batteries. Polym Int, 2019, 68: 684–693
35 Huang Z, Pan Q, Smith DM, *et al.* Plasticized hybrid network solid polymer electrolytes for lithium-metal batteries. Adv Mater Interfaces, 2019, 6: 1801445
36 Wei Z, Zhang Z, Chen S, *et al.* UV-cured polymer electrolyte for $LiNi_{0.85}Co_{0.05}Al_{0.1}O_2$//Li solid state battery working at ambient temperature. Energy Storage Mater, 2019, 22: 337–345
37 Zhang D, Zhang L, Yang K, *et al.* Superior blends solid polymer electrolyte with integrated hierarchical architectures for all-solid-state lithium-ion batteries. ACS Appl Mater Interfaces, 2017, 9: 36886–36896
38 Weston J, Steele B. Effects of inert fillers on the mechanical and electrochemical properties of lithium salt-poly(ethylene oxide) polymer electrolytes. Solid State Ion, 1982, 7: 75–79
39 Appetecchi GB, Croce F, Dautzenberg G, *et al.* Dry composite polymer electrolytes for lithium batteries. MRS Proc, 1997, 496: 511–516
40 Croce F, Settimi L, Scrosati B. Superacid ZrO_2-added, composite polymer electrolytes with improved transport properties. Electrochem Commun, 2006, 8: 364–368
41 Niu C, Liu J, Chen G, *et al.* Anion-regulated solid polymer electrolyte enhances the stable deposition of lithium ion for lithium metal batteries. J Power Sources, 2019, 417: 70–75
42 Lin D, Yuen PY, Liu Y, *et al.* A silica-aerogel-reinforced composite polymer electrolyte with high ionic conductivity and high modulus. Adv Mater, 2018, 30: 1802661
43 Liu Y, Lee JY, Hong L. Functionalized SiO_2 in poly(ethylene oxide)-based polymer electrolytes. J Power Sources, 2002, 109: 507–514
44 Xiong HM, Wang ZD, Xie DP, *et al.* Stable polymer electrolytes based on polyether-grafted ZnO nanoparticles for all-solid-state lithium batteries. J Mater Chem, 2006, 16: 1345–1349
45 Reddy MJ, Chu PP, Kumar JS, *et al.* Inhibited crystallization and its effect on conductivity in a nano-sized Fe oxide composite PEO solid electrolyte. J Power Sources, 2006, 161: 535–540
46 Zhu K, Liu Y, Liu J. A fast charging/discharging all-solid-state lithium ion battery based on PEO-MIL-53(Al)-LiTFSI thin film electrolyte. RSC Adv, 2014, 4: 42278–42284
47 Shen L, Wu HB, Liu F, *et al.* Creating lithium-ion electrolytes with biomimetic ionic channels in metal-organic frameworks. Adv Mater, 2018, 30: 1707476
48 Liu L, Lyu J, Mo J, *et al.* Flexible, high-voltage, ion-conducting composite membranes with 3D aramid nanofiber frameworks for stable all-solid-state lithium metal batteries. Sci China Mater, 2020, 63: 703–718
49 Pan Q, Zheng Y, Kota S, *et al.* 2D MXene-containing polymer electrolytes for all-solid-state lithium metal batteries. Nanoscale Adv, 2019, 1: 395–402
50 Lin Y, Wang X, Liu J, *et al.* Natural halloysite nano-clay electrolyte for advanced all-solid-state lithium-sulfur batteries. Nano Energy, 2017, 31: 478–485
51 Tang C, Hackenberg K, Fu Q, *et al.* High ion conducting polymer nanocomposite electrolytes using hybrid nanofillers. Nano Lett, 2012, 12: 1152–1156
52 Cao L, Wu H, Yang P, *et al.* Graphene oxide-based solid electrolytes with 3D prepercolating pathways for efficient proton transport. Adv Funct Mater, 2018, 28: 1804944
53 Liu W, Lee SW, Lin D, *et al.* Enhancing ionic conductivity in composite polymer electrolytes with well-aligned ceramic nanowires. Nat Energy, 2017, 2: 17035
54 Zhang X, Xie J, Shi F, *et al.* Vertically aligned and continuous nanoscale ceramic–polymer interfaces in composite solid polymer electrolytes for enhanced ionic conductivity. Nano Lett, 2018, 18: 3829–3838
55 Bae J, Li Y, Zhang J, *et al.* A 3D nanostructured hydrogel-framework-eerived high-performance composite polymer lithium-ion electrolyte. Angew Chem Int Ed, 2018, 57: 2096–2100
56 Fu KK, Gong Y, Dai J, *et al.* Flexible, solid-state, ion-conducting

membrane with 3D garnet nanofiber networks for lithium batteries. Proc Natl Acad Sci USA, 2016, 113: 7094–7099
57 Sheng O, Jin C, Luo J, *et al.* $Mg_2B_2O_5$ nanowire enabled multifunctional solid-state electrolytes with high ionic conductivity, excellent mechanical properties, and flame-retardant performance. Nano Lett, 2018, 18: 3104–3112
58 Zheng M, Wu K, Liang H, *et al.* Microstructure and mechanical properties of aluminum borate whisker-reinforced magnesium matrix composites. Mater Lett, 2002, 57: 558–564
59 Zhou D, Mei X, Ouyang J. Ionic conductivity enhancement of polyethylene oxide-$LiClO_4$ electrolyte by adding functionalized multi-walled carbon nanotubes. J Phys Chem C, 2011, 115: 16688–16694
60 Li M, Wahyudi W, Kumar P, *et al.* Scalable approach to construct free-standing and flexible carbon networks for lithium–sulfur battery. ACS Appl Mater Interfaces, 2017, 9: 8047–8054
61 Zhai H, Xu P, Ning M, *et al.* A flexible solid composite electrolyte with vertically aligned and connected ion-conducting nanoparticles for lithium batteries. Nano Lett, 2017, 17: 3182–3187
62 Porcarelli L, Shaplov AS, Bella F, *et al.* Single-ion conducting polymer electrolytes for lithium metal polymer batteries that operate at ambient temperature. ACS Energy Lett, 2016, 1: 678–682
63 Li C, Qin B, Zhang Y, *et al.* Single-ion conducting electrolyte based on electrospun nanofibers for high-performance lithium batteries. Adv Energy Mater, 2019, 9: 1803422
64 Lin D, Liu W, Liu Y, *et al.* High ionic conductivity of composite solid polymer electrolyte *via in situ* synthesis of monodispersed SiO_2 nanospheres in poly(ethylene oxide). Nano Lett, 2016, 16: 459–465
65 Angulakshmi N, Kumar RS, Kulandainathan MA, *et al.* Composite polymer electrolytes encompassing metal organic frame works: a new strategy for all-solid-state lithium batteries. J Phys Chem C, 2014, 118: 24240–24247

Acknowledgements This work was financially supported by the National Natural Science Foundation of China (51804344), the Huxiang Youth Talent Support Program (2019RS2002), the Innovation and Entrepreneurship Project of Hunan Province, China (2018GK5026), the Innovation-Driven Project of Central South University (2020CX027), and Guangdong YangFan Plan for Postdoctor Program.

Author contributions Guo X designed and engineered the samples, wrote the paper with support from Wang J. All authors contributed to the general discussion.

Conflict of interest The authors declare that they have no conflict of interest.

Supplementary information Experimental details and supporting data are available in the online version of the paper.

Xiqiang Guo obtained his BSc degree (2017) in metallurgical engineering, and then pursued his master degree (2017-2020) in Professor Xinhai Li and Associate Professor Jiexi Wang's group at Central South University (China). He mainly studies the efficient synthesis of 1D nanomaterials and their applications in enhancing the solid polymer electrolytes for lithium-ion batteries. Besides, he has been a visiting student in Zaiping Guo's group at the University of Wollongong (Australia), where he participated in the separator research for lithium–sulfur batteries.

Jiexi Wang received his BSc degree (2010) in metallurgical engineering and PhD degree (2015) in physical chemistry of metallurgy from Central South University (China). After working as a postdoctoral fellow at Hong Kong University of Science & Technology and The University of Hong Kong, he started his independent research career as an associate professor at Central South University (China) in 2017. His research focuses on the green synthesis and application of nonferrous-based materials and composites for energy storage, such as high-power/high-energy lithium/sodium ion batteries, and supercapacitors. He has published about 100 scientific papers with ~3,800 citations (h-index=38).

$Al_4B_2O_9$纳米棒改性制备优异综合性能的固体聚合物电解质

郭西强[1], 彭文杰[1,2], 吴雨琪[1], 郭华军[1,2], 王志兴[1,2], 李新海[1,2], 柯勇[1,3], 吴理觉[3], 付海阔[3], 王接喜[1,2*]

摘要 随着储能设备和电力驱动产品的激增, 特别是电动汽车的大规模推广应用, 全固态电池被认为是最有可能解决电动设备日益严峻的安全问题和高能量密度需求的策略之一. 本文报道了一种$Al_4B_2O_9$纳米棒改性的聚环氧乙烷(PEO)基固体聚合物电解质(ASPE), 其具有高离子电导率、宽电化学窗口、良好的机械性能和阻燃性能. 具体来说, 因为$Al_4B_2O_9$纳米棒与PEO之间的相互作用会产生更长距离的Li^+传递通道, 所以ASPE-1具有优异的离子电导率, 在30和60°C下, 分别达到3.1×10^{-4}和4.35×10^{-5} S cm^{-1}. 此外, ASPE-1在60°C时表现出良好的电化学稳定性, 分解电压达5.1 V. 另外, ASPE-1在$LiFePO_4$//Li半电池具有良好的循环倍率性能, 当温度为60°C、电流密度为1 C时, 经300次循环充放电后, 放电比容量为155 mA h g^{-1}. 当温度为30°C、电流密度为0.2 C时, 经90次循环充放电后, 放电比容量为125 mA h g^{-1}, 表现出良好的低温性能. 这些实验结果证明$Al_4B_2O_9$纳米棒可以有效地提高固体聚合物电解质的综合性能.

